

# An APN-Activated Chemiluminescent Probe for Image-Guided Surgery of Malignant Tumors

Yinghua Liu, Jianfeng Zeng, Qing Li,\* Minqian Miao, Zhuorun Song, Min Zhao, Qingqing Miao,\* and Mingyuan Gao\*

Developing smart molecular probes for assisting surgeons to precisely detect cancerous tissues and to completely remove all of them during the surgery is urgently required. Conventional fluorescent probes allow for tumor detection but with limited signal-to-noise ratio. Herein, an aminopeptidase N/CD13 (APN)-activated chemiluminescent probe (APN-ACLCP) is reported for sensitive imaging and precise resection of malignant tumors. The APN-ACLCP probe is based on acryl-substituted phenoxy-dioxetane that is coupled with an APN-cleavable substrate via a self-immolative linker. Upon activation by APN through specific hydrolysis reaction, APN-ACLCP generates spontaneously chemiluminescence signal, which offers a possibility to sensitively search tumors by simply spraying APN-ACLCP on the suspicious sites. Animal imaging studies reveal that a sufficient signal contrast between the cancerous tissues and the normal counterparts can be achieved within 5 min, which can allow for rapid detection and surgical resection of tumors, particularly tiny metastatic lesions in mice model, under the guidance of chemiluminescence imaging, well manifesting its potential for image-guided surgery of malignant tumors.

## 1. Introduction

Surgical resection plays a major role in cancer therapy and remains the most efficient treatment for solid tumors.<sup>[1]</sup> During surgical resection, the tumors visible to the naked eye can be removed. However, some malignant nodules including metastatic lesions of less than 3 mm are easily missing during surgery, leading to cancer recurrence.<sup>[2]</sup> Thus, sensitive detection of tiny cancerous lesions during surgery has become an imperative concern.<sup>[3]</sup>

Fluorescence imaging has been demonstrated to be one of the most attractive diagnostic approaches due to its high sensitivity, low cost, real-time signal acquisition, high spatial resolution, and noninvasive nature.<sup>[4]</sup> Accordingly, many efforts have been devoted to exploiting novel and innovative fluorescent probes suitable for image-guided surgery of tumors in the

past few decades.<sup>[5]</sup> In particular, activatable probes that can be specifically turned on to emit fluorescence by various cancerous biomarkers have been developed,<sup>[6]</sup> leading to significant improvement in the precision of tumor resection.<sup>[7]</sup> For instance, Urano et al. have developed a  $\gamma$ -glutamyltranspeptidase-responsive fluorescent probe that can light up tiny ovarian cancer nodules within 10 min<sup>[5c]</sup> and Bogyo et al. have reported a dual proteases-activated fluorescent probe with improved specificity and sensitivity in localizing lung cancer metastases of <1 mm in diameter.<sup>[8]</sup> In spite of these encouraging advances, fluorescence imaging always suffers from some inherent limitations including photobleaching, shallow tissue-penetration-depth, and high background signal arising from the autofluorescence of biological tissues upon light excitation.

In this context, developing new strategies for creating luminescent probes with improved specificity and accuracy in discriminating cancerous lesions from normal tissues during the surgery is fundamentally important.<sup>[9]</sup>

Chemiluminescence has been regarded as an alternative choice of constructing sensitive probes for biosensing and imaging.<sup>[10]</sup> Unlike fluorescence, chemiluminescence utilizes chemical reactions rather than photoexcitation to trigger the luminescence. As a consequence, chemiluminescence imaging can remarkably suppress the interference of autofluorescence to give rise to higher signal-to-noise ratio and better sensitivity for tumor detection in comparison with conventional fluorescence imaging.<sup>[11]</sup> As an attempt, Ding et al. have reported a chemiluminescent dioxetane-based nanoparticle for image-guided cancer surgery,<sup>[12]</sup> but it is an “always-on” probe, which has poor specificity and high background compared to activatable probe, and thus is unfavorable for tumor detection during a surgical practice. In recent years, a series of activatable chemiluminescent probes based on Schaap’s dioxetanes have been developed for selective detection and imaging of various biomarkers such as cathepsin B, nitroreductase,  $\beta$ -galactosidase, reactive species, granzyme B and aminopeptidases, both in vitro and in vivo.<sup>[13]</sup> However, existing activatable chemiluminescent probes have not been explored for image-guided tumor surgery.

Aminopeptidase N/CD13 (APN), a transmembrane metalloprotease that can preferentially hydrolyze N-terminal alanine from polypeptides, is the most studied cancer-related aminopeptidase.<sup>[14]</sup> Plentiful studies have demonstrated that APN is

Y. Liu, J. Zeng, Q. Li, M. Miao, Z. Song, M. Zhao, Q. Miao, M. Gao  
Key Laboratory of Radiation Medicine and Protection  
School for Radiological and Interdisciplinary Sciences (RAD-X)  
Collaborative Innovation Center of Radiation Medicine of Jiangsu Higher  
Education Institutions  
Soochow University  
Suzhou 215123, P. R. China  
E-mail: qli87@suda.edu.cn; qqmiao@suda.edu.cn; gaomy@suda.edu.cn

 The ORCID identification number(s) for the author(s) of this article can be found under <https://doi.org/10.1002/adom.202102709>.

DOI: 10.1002/adom.202102709

overexpressed on the surface of many tumor cells and associated with the invasion, angiogenesis, and metastasis of different human cancers, making it a promising target for tumor diagnosis.<sup>[15]</sup> Therefore, constructing APN-specific imaging probes can potentially improve the detection sensitivity of tiny tumors and metastases. To the best of our knowledge, no APN-activated chemiluminescent probes have been reported, with exception of some APN-activated fluorescent probes.<sup>[16]</sup> Towards precise cancerous tissue resection, herein we report an APN-specific chemiluminescent probe that can be triggered to emit chemiluminescence through a one-step hydrolysis reaction catalyzed by APN. The activatable chemiluminescent properties were studied both in vitro and in mice carcinoma models in vivo. Most importantly, the instant response to small tumors and unobvious metastatic lesions was demonstrated by directly spraying the activatable probe on the surface of suspicious tissues, to show the advantages of the rational combination of chemiluminescence with APN specific activation for rapid and accurate cancer detection.

## 2. Results and Discussion

### 2.1. Design and Synthesis of APN-Activated Chemiluminescent Probe

In order to specifically and sensitively detect APN, an activatable chemiluminescent APN probe, comprising an APN-responsive amino acid substrate L-alanine,<sup>[17]</sup> a self-immolative spacer p-aminobenzyl alcohol (PABA), and a highly emissive acryl-substituted phenoxy-dioxetane moiety, was constructed. The PABA spacer between the amino acid substrate and the acryl-substituted phenoxy-dioxetane is introduced to reduce the steric hindrance of the latter for facilitating the interaction of APN with the amino acid segment of the APN-activated chemiluminescent probe (APN-ACLCP). Upon cleavage of the amino acid segment by APN, as shown in **Figure 1a**, a spontaneous 1,6-elimination within the PABA spacer of APN-ACLCP will occur, causing the release of the unmasked dioxetane that will subsequently be deprotonated under physiological conditions to further decompose into cleaved dioxetane through a chemiexcitation process, which is accompanied by light emission at 540 nm.<sup>[12a]</sup> In this way, the APN-specific activatable probe hopefully with higher imaging sensitivity was designed.

The detailed synthetic procedures for APN-ACLCP probe are provided in Scheme S1 (Supporting Information). The chemical structures of all intermediates and the final compound APN-ACLCP were systematically characterized by nuclear magnetic resonance (<sup>1</sup>H NMR, <sup>13</sup>C NMR), matrix-assisted laser desorption/ionization time of flight mass spectrometry, and high-resolution mass spectrometry (HR-MS) with all data given in Figure S1–S6 (Supporting Information). In brief, all these measurements demonstrated that the APN-ACLCP was successfully synthesized.

### 2.2. In Vitro Studies of APN-ACLCP

To characterize the specific responsiveness of APN-ACLCP, optical spectroscopy and high-performance liquid

chromatography were employed to monitor the structural variation of APN-ACLCP induced by APN. In detail, the chemiluminescence of APN-ACLCP incubated with recombinant human APN was first monitored in phosphate buffer (1 × PBS) containing 5% dimethyl sulfoxide (DMSO) at 37 °C. As shown in **Figure 1b**, an obvious chemiluminescence signal appears very quickly in response to APN and reaches its intensity maximum at 20 min postincubation, followed by a slow decrease in signal intensity. As expected, the characteristic emission of dioxetane centered at 540 nm was recorded as shown in **Figure S7** (Supporting Information), while almost no chemiluminescence signal was observed in the absence of APN, giving rise to an on/off ratio of approximately 190:1. The APN-induced structural variations were further investigated by absorption and fluorescence spectroscopy by comparing the spectra of APN-ACLCP recorded before and after incubation with APN. **Figure 1c,d** reveals that APN-ACLCP presents nearly no fluorescence, and shows weak and almost featureless absorption above 350 nm before subjected to incubation with APN. After incubation with APN, the probe however exhibits a strong fluorescence peaking at 540 nm under excitation at 400 nm, accompanied by the appearance of a new absorption band at around 400 nm. The high-performance liquid chromatography (HPLC) results in **Figure 1e** further reveal that the retention time of APN-ACLCP was shifted from 23.6 to 19.1 min after APN-ACLCP was incubated with APN, indicating that APN-ACLCP was hydrolyzed and converted to cleaved dioxetane ( $m/z = 269.0224$ , [M-H]<sup>-</sup>) according to the HR-MS result shown in **Figure S8** (Supporting Information). To assess the responsive specificity, the chemiluminescence of APN-ACLCP was also carefully investigated in the presence of bestatin (BT), an inhibitor of APN, and different types of species possibly involved in tumor microenvironment as well. As shown in **Figure 1f**, only APN can trigger the chemiluminescence out of APN-ACLCP, while the emission intensity is decreased by more than 97% in case BT is present, well manifesting the excellent specificity of APN-ACLCP in response to APN. In addition, the pH effect on the responsiveness of APN-ACLCP was also investigated. The results displayed in **Figure 1g** reveal that the pH value of the solution exhibited substantial impacts on the chemiluminescence of APN-ACLCP, particularly in a pH of 6.0–8.0 in presence of APN, well covering the physiological pH and acidic pH environment of solid tumors. In contrast, in this pH range, very weak chemiluminescence emission and neglectable pH effects are presented in the absence of APN.

The detection sensitivity was then determined after APN-ACLCP was incubated with APN of different concentrations for 20 min. As displayed in **Figure 2a,b**, the intensity of chemiluminescence of APN-ACLCP remarkably increases against the concentration of APN. Through a linear fitting of the correlation between the chemiluminescence intensity and APN concentration, an APN detection limit of 0.056 ng mL<sup>-1</sup> was derived, 20-fold lower than that determined through fluorescence under the identical conditions indicated in **Figure S9** (Supporting Information). It is also lower than that of most previously reported APN-responsive fluorescent probes in **Table S1** (Supporting Information). The lowered detection limit is apparently more favorable for ultrasensitive detection of tiny lesions through APN.

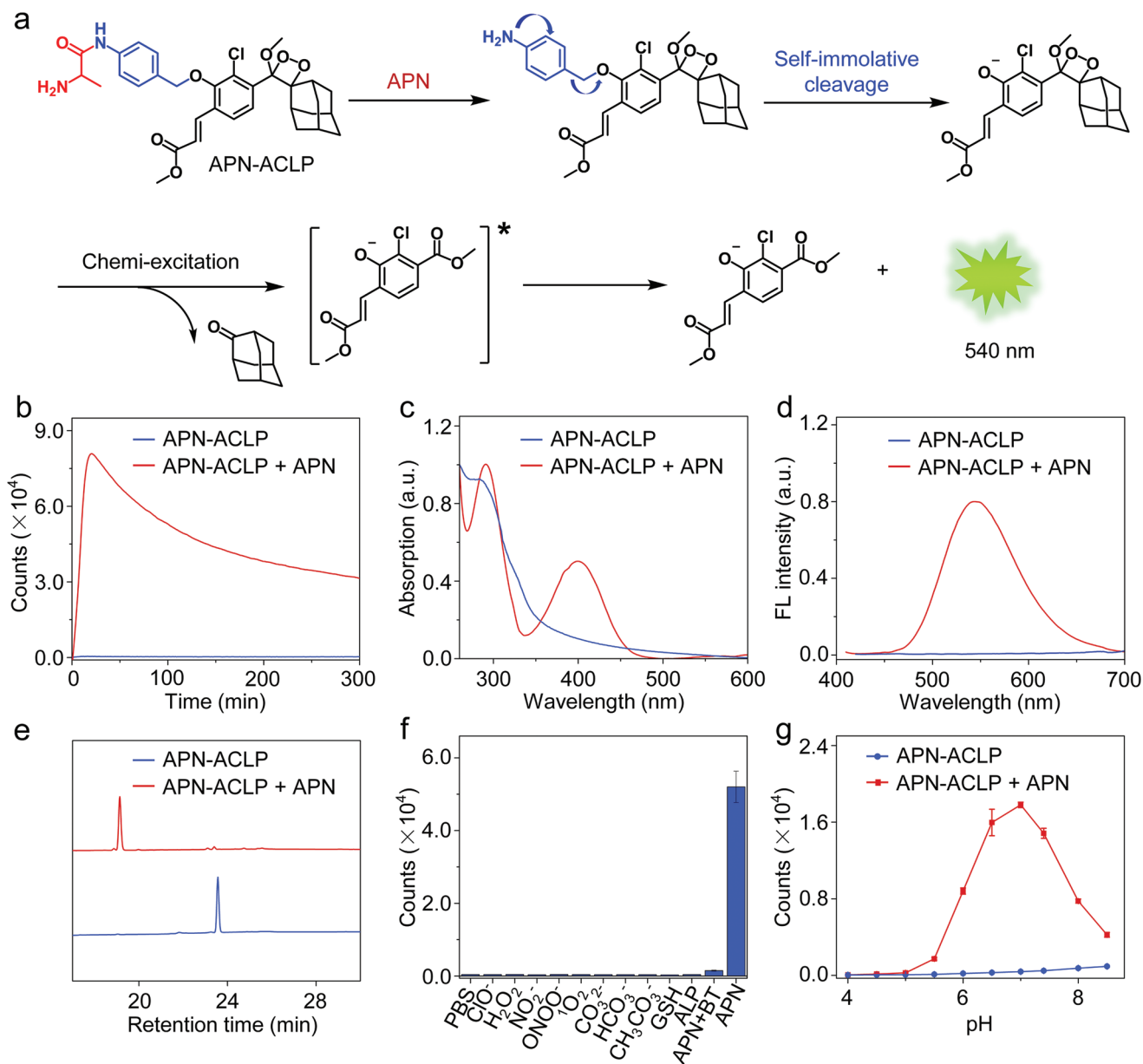


**Figure 1.** In vitro evaluation of APN-ACLIP. a) Chemical structure of APN-ACLIP and the corresponding mechanism of APN detection. b) Temporal evolutions of the chemiluminescence of APN-ACLIP ( $10 \times 10^{-6}$  M) in the absence or presence of APN of  $200 \text{ ng mL}^{-1}$  at  $37^\circ\text{C}$ . c,d) Normalized absorption and fluorescence spectra of APN-ACLIP recorded in the absence or presence of APN ( $200 \text{ ng mL}^{-1}$ ) after incubation for 10 h at  $37^\circ\text{C}$  in  $1 \times$  PBS buffer containing 5% DMSO. The fluorescence spectra were captured under excitation at 400 nm. e) HPLC traces of APN-ACLIP before or after incubation with APN. f) The chemiluminescence intensity of APN-ACLIP ( $10 \times 10^{-6}$  M) recorded after incubation with  $\text{ClO}_2^-$ ,  $\text{H}_2\text{O}_2$ ,  $\text{NO}_2^-$ ,  $\text{ONOO}^-$ ,  $^1\text{O}_2$ ,  $\text{CO}_3^{2-}$ ,  $\text{HCO}_3^-$ ,  $\text{CH}_3\text{CO}_3^-$ , and GSH of  $100 \times 10^{-6}$  M, ALP of  $100 \text{ U L}^{-1}$ , APN of  $100 \text{ ng mL}^{-1}$ , respectively, in  $1 \times$  PBS buffer for 20 min at  $37^\circ\text{C}$ . For the inhibition experiment, the concentration of BT was of  $200 \times 10^{-6}$  M. g) Chemiluminescence of APN-ACLIP in  $1 \times$  PBS with different pH for 20 min at  $37^\circ\text{C}$  in the absence or presence of APN. The error bars represent the standard deviation ( $n = 3$ ).

To evaluate the performance of APN-ACLIP in vivo, the tissue penetration depth of the chemiluminescence triggered by APN was determined by measuring the luminescence intensity through chicken breast tissues of different thicknesses with IVIS system. As displayed in Figure 2c, both chemiluminescence and fluorescence signals dramatically decrease against chicken tissue thickness. However, the chemiluminescence signal remains detectable even when the tissue thickness is

raised up to 20 mm. In huge contrast, as shown in Figure 2d, the fluorescence signal is hardly detectable although the tissue thickness is only 5 mm, showing a signal-to-noise ratio (SNR) of  $1.14 \pm 0.05$  much lower than that for chemiluminescence, i.e.,  $174.2 \pm 30.2$ . The much higher tissue penetration depth of chemiluminescence is mainly caused by the poor penetration depth of the excitation light of 430 nm for fluorescence, while greater SNR of chemiluminescence can be attributed to the

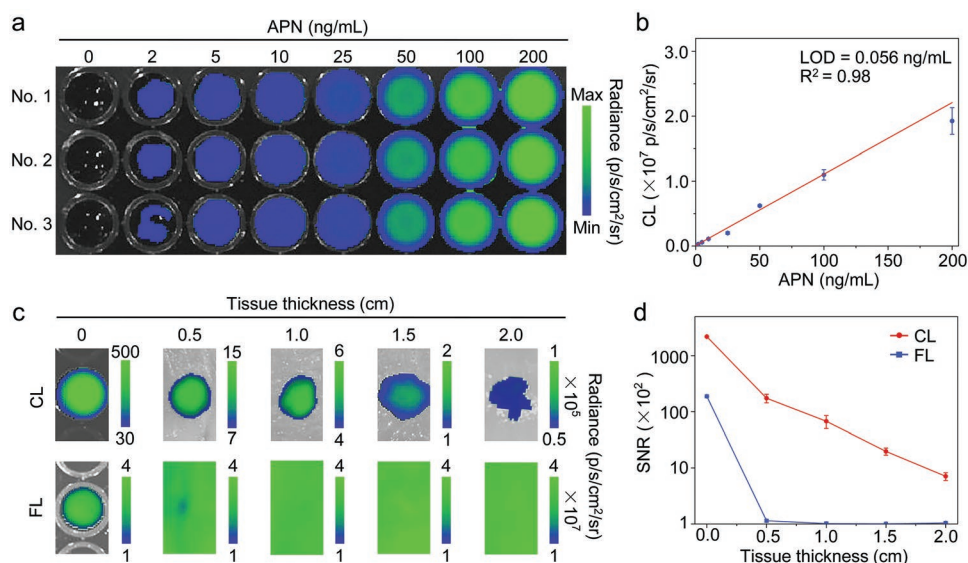


**Figure 2.** Comparison of the chemiluminescence (CL) and fluorescence (FL) of APN-ACLP through tissues of different thicknesses. a) Chemiluminescence images of APN-ACLP ( $10 \times 10^{-6}$  M) in the presence of different concentrations of APN (0–200 ng mL<sup>-1</sup>) captured for incubation of 20 min at 37 °C in 1 × PBS buffer containing 5% DMSO. b) A linear fitting of the relationship between CL intensity and APN concentration. c) Chemiluminescence and fluorescence images of APN-ACLP in the presence of APN captured through chicken tissues with different thicknesses on IVIS spectrum imaging system. The excitation wavelength for fluorescence imaging was 430 nm. d) SNR of chemiluminescence and fluorescence of APN-ACLP against the tissue thickness derived from the results given in panel (c). The error bars represent the standard deviation ( $n = 3$ ).

extremely low background of chemiluminescence, well manifesting the advantages of chemiluminescence over fluorescence with respect to in vivo imaging applications.

Before further in vivo imaging experiments, the cytotoxicity of APN-ACLP was evaluated through CCK-8 assay against HepG2 hepatoma carcinoma cells, LO2 normal human liver cells, and 4T1 mammary gland carcinoma cells, respectively. The results in Figure S10 (Supporting Information) suggested that APN-ACLP probe exhibited no obvious cytotoxicity against the aforementioned cells. Then, the responsiveness of APN-ACLP to APN expressed by HepG2 cells and LO2 cells, respectively, was compared after being incubated with these cells. As shown in Figure S11a (Supporting Information), HepG2 cells exhibited much stronger chemiluminescence than LO2 cells, owing to the much higher expression level of APN in HepG2 cells. Nevertheless, the chemiluminescence was dramatically suppressed if the HepG2 cells were pre-treated with BT, the inhibitor of APN, well demonstrating the outstanding specificity of APN-ACLP in react to APN-overexpressed HepG2 cells (Figure S11b, Supporting Information).

### 2.3. Chemiluminescence Imaging of APN-Overexpressed Tumor In Vivo

Inspired by the sensitive chemiluminescence response towards APN in vitro, we then investigated the performance of APN-ACLP in response to endogenous APN in vivo. Mice bearing HepG2 xenograft tumor were imaged through both chemiluminescence and fluorescence, respectively, after APN-ACLP was intratumorally injected. The imaging results are provided in Figure 3a and the signal intensities of chemiluminescence of the tumorous sites were recorded and provided in Figure 3b.

The chemiluminescence signal intensity rapidly increases and reaches its maximum at about 10 min post-injection. The following decline lasts over 60 min with SNR remaining around 250, as shown in Figure 3c. However, the SNR of fluorescence images is much lower due to the autofluorescence of the tissues under photoexcitation. Furthermore, the chemiluminescence signal intensity was remarkably suppressed if the APN inhibitor BT was pre-injected into HepG2 xenograft tumor. All these data clearly demonstrate that the APN-ACLP can be used for rapid and noninvasive detection of APN-overexpressed tumors in vivo.

### 2.4. Chemiluminescence Image-Guided Surgery

The high SNR and quick response to APN in vivo encouraged us to use APN-ACLP for discerning tumor tissues from normal tissues by directly spraying its aqueous solution on the surface of resected HepG2 xenograft tumor ex vivo, with normal liver tissues serving as control. In striking comparison with normal liver tissue, as shown in Figure 4a,b, the maximum tumor-to-normal tissue ratio for chemiluminescence is around 160 at 10 min, significantly higher than fluorescence as expected. These data reveal that APN-ACLP holds the ability to distinguish tumors from normal tissues through simple spraying and may provide a promising tool for precise tumor resection.

The feasibility of the chemiluminescent probe for image-guided tumor resection was then demonstrated in orthotopic HepG2-tumor mice model. The results given in Figure S12a,b (Supporting Information) revealed that 5 min was enough to light up the tumor site, while the strong luminescent signal lasted for more than 40 min, which is long enough for removing the identified tumors apart from the fact that the tumors can

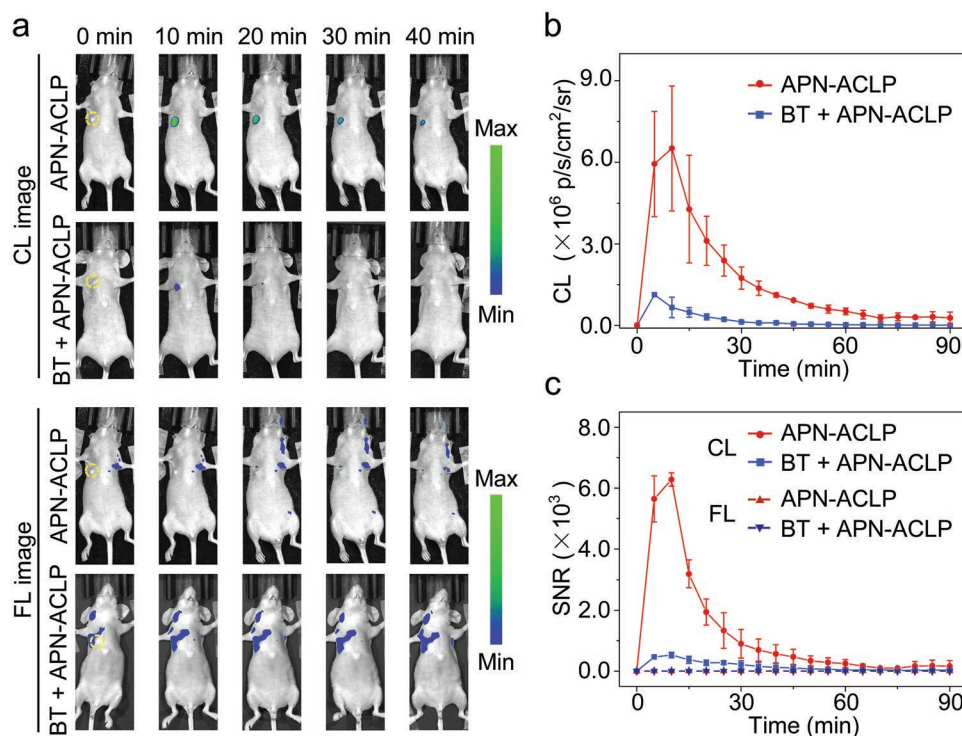


**Figure 3.** Chemiluminescence imaging of APN-overexpressed tumors in vivo. a) Representative chemiluminescence (top) and fluorescence images (bottom) of the same HepG2 xenograft recorded at different time points after the intratumoral injection of APN-ACLCP of 25  $\mu$ L or BT of 10  $\mu$ L ( $0.5 \times 10^{-3}$  M) 0.5 h prior to the injection of APN-ACLCP. b) Temporal chemiluminescence signal of the tumor site recorded after administration of APN-ACLCP in the absence or presence of BT. c) SNR of chemiluminescence and fluorescence of the tumor site recorded after administration of APN-ACLCP in the absence or presence of BT, as shown in panel (a). The fluorescence SNR trace for APN-ACLCP was covered by that for BT + APN-ACLCP. The error bars represent the standard deviation ( $n = 3$ ). The APN-ACLCP solution used for the above experiments contained  $10 \times 10^{-6}$  M APN-ACLCP in  $1 \times$  PBS with 5% DMSO.

be lit up repeatedly upon multiple sprays. Under the guidance of the chemiluminescence, a nodule from the living mouse was resected by using a scalpel. Then the resected nodule was analyzed by the hematoxylin and eosin (H&E) staining (Figure 4c). It is worth noticing that the resected nodule exhibits bright chemiluminescence after receiving secondary spraying of APN-ACLCP solution, while the original luminescent site presents no chemiluminescence at all, indicating the successfulness of the image-guided surgery.

It is well-known that malignant tumor metastasis is the pivotal cause of cancer treatment failure. However, the tiny metastatic foci are easily missing by the naked eyes during surgery. It is thus interesting to evaluate the potential of APN-ACLCP for visualizing the tiny metastases in virtue of its excellent sensitivity and superior SNR in detecting orthotopic liver cancer. To this end, a peritoneal metastasis mouse model was constructed. After the abdominal cavity was incised, the solution of APN-ACLCP was sprayed. After 10 min, the tissues showing strong chemiluminescence signals as presented in Figure 4d were resected under the guidance of chemiluminescence. The five doubtful nodules harvested were subjected to further analysis through H&E staining. The H&E staining images given in Figure 4e reveal that these nodules are metastatic lesions and the smallest one is less than 1 mm in diameter. In addition, similar experiments on the detection of hepatic and splenic metastasis of 4T1 breast cancer also provided similar results, as shown in Figures S13 and S14 (Supporting Information),

further verifying the excellent potential of APN-ACLCP for precise metastasis detection and surgery.

### 3. Conclusion

In conclusion, we have successfully developed a molecular agent APN-ACLCP that can be specially activated by cancer-associated enzyme APN to emit chemiluminescence for tumor detection and image-guided surgical resection. In comparison with the counterparts based on fluorescence, APN-ACLCP shows superior signal-to-noise ratio and remarkably improved tissue penetration depth. By virtue of these outstanding properties, the APN-ACLCP is applied to sensitively discern APN-overexpressed tumorous tissues from the normal tissues. Via simple spraying, the tiny tumors and metastatic lesions can be lit up to show chemiluminescence with exceptionally high signal-to-noise ratios, allowing for precise resection under the guidance of the chemiluminescence. To the best of our knowledge, we herein provide the first activatable chemiluminescent probe for image-guided surgical resection of tumor through simple spraying and believe that the probe design strategy holds remarkable potential for clinical applications. Given that the near-infrared (NIR) region is superior for in vivo imaging due to the improved tissue penetration and reduced light scattering,<sup>[18]</sup> our further work is underway to design the APN-activated NIR chemiluminescent probes.

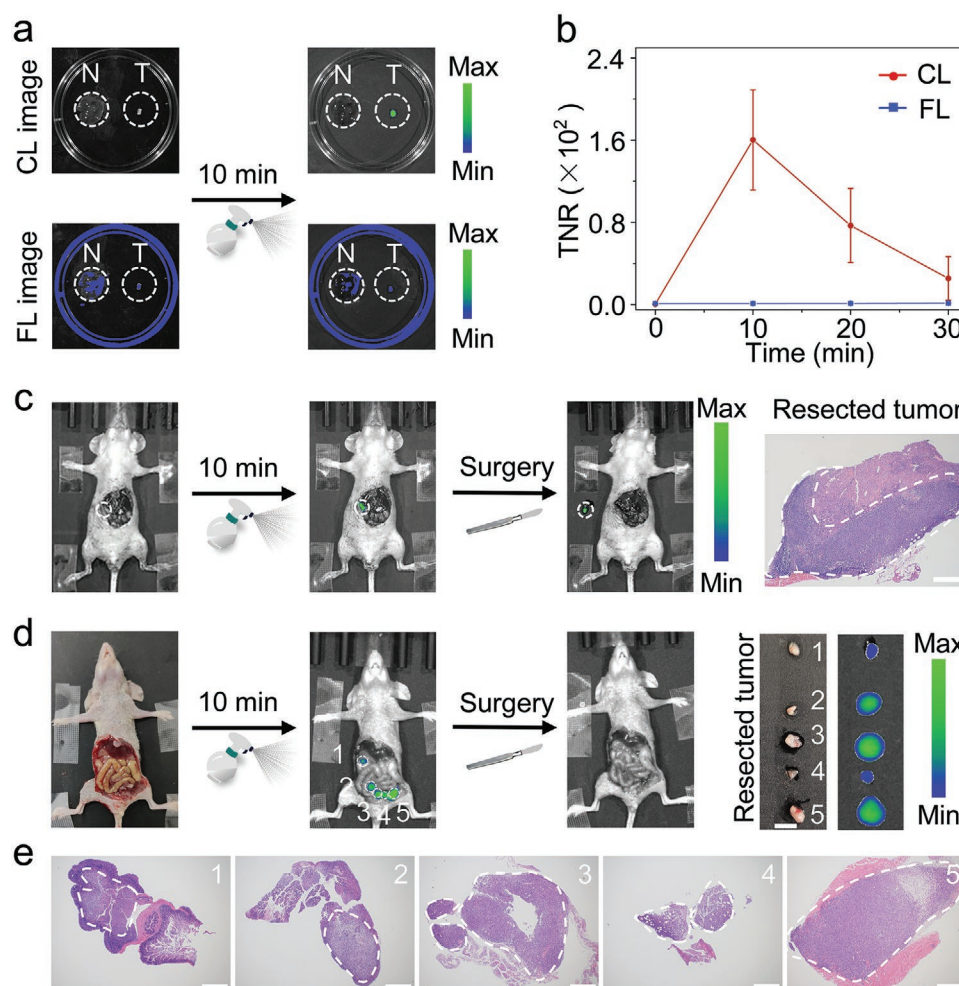


**Figure 4.** Chemiluminescence image-guided surgery. a) Chemiluminescence and fluorescence images of HepG2-tumors (T) and normal liver tissues (N) recorded before and 10 min after being exposed to APN-ACLP spray. b) Tumor to normal tissue ratio (TNR) obtained according to the results given in panel (a). The error bars represent the standard deviation ( $n = 3$ ). c) Chemiluminescence image-guided surgery of orthotopic HepG2-tumors in mice. The H&E staining results of resected tumor on the right. The scale bar represents 500  $\mu\text{m}$ . d) Bright field images or overlaid with chemiluminescence images recorded before and 10 min after spraying APN-ACLP on the suspicious tumor site, together with the tiny metastases lesions resected under the guidance of chemiluminescence. The scale bar represents 5 mm. e) H&E staining results of the resected tumors in panel (d). Scale bar = 500  $\mu\text{m}$ . The APN-ACLP solution used for the above experiments contained  $10 \times 10^{-6}$  M APN-ACLP in  $1 \times$  PBS with 5% DMSO.

#### 4. Experimental Section

**Materials:** All chemicals and reagents purchased were analytical grade and used without further purification, unless otherwise stated. Fmoc-L-Ala-OH, 1-hydroxybenzotriazole hydrate (HOBT), *N,N,N',N'*-tetramethyl-O-(1H-benzotriazol-1-yl)uranium hexafluorophosphate (HBTU) were purchased from GL Biochem (Shanghai, China). Aminopeptidase N/CD13 (APN) was obtained from R&D Systems. Bestatin (BT), an inhibitor of APN, was purchased from Aladdin. Alkaline phosphatase (ALP) was obtained from BaoMan Inc. (Shanghai, China). Fetal bovine serum (FBS) was purchased from HyClone. Roswell Park Memorial Institute (RPMI) 1640 medium and Dulbecco's modified eagle medium (DMEM) were purchased from BasalMedia. Lysotracker and Mitotracker were purchased from Beyotime Bio tech. Hoechst 33342 reagent and phosphate buffer saline (PBS) were purchased from Solarbio Biotech. Cell counting kit-8 (CCK-8) was purchased from APEX BIO. Water was supplied by Milli-Q Integral10 (Millipore Corporation, Bedford, USA).

**Characterization:** High performance liquid chromatography (HPLC) analyses were performed on Waters Alliance E2695 system equipped with E2695 separation module, 2489 UV detector and a Water X Bridge

C18 ( $4.6 \times 250$  mm, 5  $\mu\text{m}$ ) column with  $\text{CH}_3\text{OH}$  (0.1% of TFA) and water (0.1% of TFA) as the eluent. HPLC purification was performed on an Elite P3500 gradient preparative system equipped with P3500 pump, UV detector (UV3100) and a CST Daiso C18 ( $20 \times 250$  mm) column with  $\text{CH}_3\text{OH}$  (0.1% of TFA) or  $\text{CH}_3\text{CN}$  (0.1% of TFA) and water (0.1% of TFA) as the eluent. Nuclear magnetic resonance (NMR) spectra ( $^1\text{H}$  NMR,  $^{13}\text{C}$  NMR) were recorded on a Bruker Avance NEO II 400 MHz NMR. The matrix assisted laser desorption/ionization time-of-flight mass spectrometry (MALDI-TOF-MS) spectra were obtained on a Ultraflextreme. High resolution electrospray ionization mass spectra (HR-MS) were measured at a Thermo Scientific Q Exactive instrument (Bremen, Germany) equipped with a standard ESI source. The HR-MS and MALDI-TOF-MS were reported in units of mass per charge ratio ( $m/z$ ). UV-vis spectra were recorded on a PerkinElmer Lambda 35 UV-vis spectrometer variable bandwidth. Chemiluminescence and fluorescence spectra were obtained on an Edinburgh FLS980 spectrofluorometer. The intensity of chemiluminescence in solution or cells were acquired on a microplate reader (EnSpire Multilabel Reader 2300, PerkinElmer). Chemiluminescence and fluorescence imaging were carried out using an IVIS Spectrum imaging system (PerkinElmer, Inc.).

**Synthesis of Compound C:** Compound A and compound B were synthesized according to the reported literature.<sup>[13a,17a]</sup> Compound B (31 mg, 0.08 mmol) was added to a mixture of compound A (57 mg, 0.120 mmol), NaI (45 mg, 0.3 mmol), and K<sub>2</sub>CO<sub>3</sub> (21 mg, 0.15 mmol) in anhydrous DMF (2 mL) under a nitrogen atmosphere. The reaction solution was stirred at room temperature for 6 h and monitored by TLC (hexane: ethyl acetate = 2:1). After completion, ethyl acetate (20 mL) was added to the reaction solution and was washed with deionized water (20 mL × 3). The organic phase was separated, dried over Na<sub>2</sub>SO<sub>4</sub>, filtered and evaporated. The crude product was purified with column chromatography on silica gel to obtain the product C (33.1 mg, 52.5%). <sup>1</sup>H NMR (400 MHz, CDCl<sub>3</sub>): δ = 8.35 (br, 1 H), 7.90 (d, J = 16.2 Hz, 1 H), 7.76 (d, J = 7.5 Hz, 2 H), 7.59–7.51 (m, 4 H), 7.43–7.37 (m, 5 H), 7.29 (t, J = 7.3 Hz, 2 H), 7.07 (d, J = 8.0 Hz, 1 H), 6.43 (d, J = 16.2 Hz, 1 H), 5.40 (br, 1 H), 4.97 (d, J = 4.2 Hz, 2 H), 4.46 (m, 3 H), 4.22 (t, J = 6.8 Hz, 1 H), 3.79 (s, 3 H), 3.33 (s, 3 H), 3.28 (s, 1 H), 2.07–1.66 (m, 13 H), 1.48 (d, J = 6.7 Hz, 3 H). <sup>13</sup>C NMR (100 MHz, CDCl<sub>3</sub>): δ = 166.7, 153.2, 143.2, 140.9, 139.0, 138.5, 137.8, 132.0, 129.3, 127.4, 126.7, 124.5, 119.4, 75.3, 66.9, 56.8, 51.4, 46.7, 38.6, 38.2, 36.7, 33.1, 31.5, 29.4, 29.0, 22.9, 22.3, 18.0, 13.7. MALD-TOF-MS: calcd for C<sub>47</sub>H<sub>47</sub>ClN<sub>2</sub>O<sub>7</sub>Na [M+Na]<sup>+</sup>: 809.30; found: 809.40.

**Synthesis of APN-ACLP:** Compound C (30 mg, 0.038 mmol) was dissolved in DMF (1 mL) and diethylamine (0.25 mL) was added. The mixture was stirred at room temperature for 1 h and monitored by analytical HPLC (Table S2, Supporting Information). After reaction completion, the solvent was evaporated under reduced pressure and the residue was dissolved in CH<sub>2</sub>Cl<sub>2</sub> (10 mL). Methylene blue (3 mg) was added and oxygen was bubbled through the solution while irradiating with a white light. The reaction solution was monitored by analytical HPLC. After completion, the solvent was removed under reduced pressure and the crude product was purified with preparative HPLC (Table S3, Supporting Information) to give APN-ACLP as a white solid (14 mg, 62%). <sup>1</sup>H NMR (400 MHz, CDCl<sub>3</sub>, δ): 9.84 (s, 1 H), 7.88 (d, J = 8.2 Hz, 1 H), 7.77 (d, J = 16.3 Hz, 1 H), 7.57–7.40 (m, 3 H), 7.30 (d, J = 6.6 Hz, 2 H), 6.41 (d, J = 16.0 Hz, 2 H), 4.83 (s, 2 H), 4.36 (br, 1 H), 3.74 (s, 3 H), 3.18 (s, 3 H), 3.00 (s, 1 H), 1.93–1.42 (m, 16 H). <sup>13</sup>C NMR (100 MHz, CDCl<sub>3</sub>): δ = 167.5, 154.2, 138.7, 137.5, 135.4, 132.2, 131.4, 129.7, 125.2, 120.5, 111.7, 96.3, 75.9, 52.0, 49.7, 47.0, 39.3, 36.3, 33.6, 31.9, 31.5, 29.7, 27.5, 26.1, 25.8, 23.3, 22.7, 17.2, 14.1. HR-MS: calcd for C<sub>32</sub>H<sub>38</sub>ClN<sub>2</sub>O<sub>7</sub> [M+H]<sup>+</sup>: 597.2368; found: 597.2339.

**Kinetic Measurements:** The APN-ACLP solutions (10 × 10<sup>-6</sup> M, 100 μL) with or without APN (200 ng mL<sup>-1</sup>) was incubated in 1 × PBS buffer containing 5% DMSO at 37 °C, and the real-time chemiluminescence was recorded on the microplate reader every 1 min, last for 300 min, with the integration time of 1 s, under luminescence mode.

**Studies of APN Activation, Sensitivity, and Selectivity:** APN-ACLP in black 96-well plate was incubated with APN at 37 °C in 1 × PBS buffer containing 5% DMSO. After incubation at indicated time, fluorescence spectra, chemiluminescence spectra, UV-vis spectra, fluorescence images, and chemiluminescence images of these solution were recorded and then the incubation mixture was further analyzed by HPLC. For sensitivity, APN-ACLP (10 × 10<sup>-6</sup> M, 100 μL) was incubated with different concentrations of APN (0, 2, 5, 10, 25, 50, 100, 200 ng mL<sup>-1</sup>) at 37 °C for 20 min. Chemiluminescence images were captured using the IVIS Spectrum imaging system under bioluminescence mode, with 0.75 s exposure time with an open filter. Fluorescence images were captured using the IVIS Spectrum imaging system under fluorescence mode, with excitation at 430 nm and emission filter of 540 nm. The detection limit was determined from emission intensities according to the equation: 3δ/k, where δ represents the standard deviation of blank, and k represents the slope of plot of intensities. For selectivity, APN-ACLP (10 × 10<sup>-6</sup> M, 100 μL) was incubated with ClO<sup>-</sup>, H<sub>2</sub>O<sub>2</sub>, NO<sub>2</sub><sup>-</sup>, ONOO<sup>-</sup>, <sup>1</sup>O<sub>2</sub>, CO<sub>3</sub><sup>2-</sup>, HCO<sub>3</sub><sup>-</sup>, CH<sub>3</sub>CO<sub>3</sub><sup>-</sup>, and GSH of 100 × 10<sup>-6</sup> M, ALP of 100 U L<sup>-1</sup>, APN of 100 ng mL<sup>-1</sup>, respectively, in 1 × PBS buffer for 20 min at 37 °C. The chemiluminescence of each solution was recorded on the microplate reader with 1 s of integration time, under luminescence mode. ONOO<sup>-</sup> and <sup>1</sup>O<sub>2</sub> were prepared according to the reported literature.<sup>[19]</sup>

**Tissue-Penetration Measurement:** APN-ACLP (10 × 10<sup>-6</sup> M, 200 μL) in black 96-well plate was incubated with APN (200 ng mL<sup>-1</sup>) in 1 × PBS buffer containing 5% DMSO. After incubation for 20 min at 37 °C, the solution wells were covered by the chicken breast tissue with different thickness (0, 5, 10, 15, 20 mm). Chemiluminescence images were captured using the IVIS Spectrum imaging system under bioluminescence mode, with 60 s exposure time under open filter. Fluorescence images were captured using the IVIS Spectrum imaging system under fluorescence mode, with excitation at 430 nm and emission filter of 540 nm. The signal-to-noise ratio (SNR) was calculated as SNR = emission intensities/background, where background refers to the signal intensity of neighboring tissues.

**Cell Incubation:** HepG2 cells were cultured in DMEM (BasalMedia) supplemented with 10% (v/v) FBS (fetal bovine serum, HyClone) and 1% (v/v) penicillin/streptomycin antibiotics. 4T1 and LO2 cells were cultured in RPMI medium 1640 (BasalMedia) supplemented with 10% FBS and 1% penicillin/streptomycin antibiotics. All cells were treated at 37 °C under a humidified atmosphere containing 5% CO<sub>2</sub> and 95% humidified air. The medium was changed every other day.

**Cell Cytotoxicity Experiment:** Cells were seeded in 96-well plates (6 × 10<sup>3</sup> cells in 100 μL per well) and allowed to grow for 24 h. The medium was removed, and the cells were incubated with APN-ACLP (0, 5, and 10 × 10<sup>-6</sup> M, 100 μL per well) for 12 h. The medium was changed and the cells were incubated with CCK-8 (0.5 mg/mL) for another 1 or 1.5 h. The absorbance of CCK-8 at 450 nm was measured by using a microplate reader (Bio Tek, Synergy 2). Cell viability was expressed by the ratio of the absorbance of the cells incubated with probe solution to that of the cells incubated with culture medium only.

**Chemiluminescence Imaging for Cells:** Cells were seeded in black 96-well plates (6 × 10<sup>3</sup> cells in 100 μL per well) and allowed to grow for 24 h. The medium was removed and the cells were incubated with APN-ACLP (10 × 10<sup>-6</sup> M, 100 μL per well) at 37 °C for 30 min. For the inhibiting study, HepG2 cells were treated with APN inhibitor BT (0.5 × 10<sup>-3</sup> M) for 30 min, and then incubated with APN-ACLP at 37 °C for 30 min. Chemiluminescence images were captured using the IVIS Spectrum imaging system under bioluminescence mode, with 10 s exposure time with an open filter.

**Animal Model:** All mice were experimented in accordance with guidelines approved by the ethics committee of Soochow University (Suzhou, China), and the approval number is 202104A0107. Specific pathogen free (SPF) grade BALB/c nude mice and BALB/c mice (3–5 weeks old) were provided by the laboratory of the Animal Center of Soochow University. The xenograft tumor models were established by subcutaneous injection of HepG2 cells (2 × 10<sup>6</sup> cells in 50 μL 1 × PBS) into the armpit region. The tumor imaging was carried out on 7–10 d after the inoculation of tumor cells. The orthotopic tumor models were established through the injection of HepG2 cells (8 × 10<sup>5</sup> cells in 20 μL 1 × PBS) into the right lobe of mice liver within the period of mice anesthesia. The growth of tumor was observed by an MRS 3000 model (MR Solution, Britain), and the size of orthotopic liver tumor was depicted by T<sub>2</sub>-weighted imaging. The orthotopic HepG2 tumor-bearing mice were experimented on 7 d after the inoculation of tumor cells. For the peritoneal metastasis model, 4T1 murine breast cancer cells (2 × 10<sup>6</sup> cells in 200 μL 1 × PBS) were intraperitoneally injected into female nude mice. After about 5–7 d, the peritoneal metastasis model was established. The hepatic and splenic metastasis models of breast cancer were established by subcutaneous injection of 4T1 cells (2 × 10<sup>6</sup> cells in 50 μL 1 × PBS) into the mammary gland of BALB/c mice. After about 4 weeks, the mice were euthanized and their liver and spleen samples were moderately taken out from body.

**Visualization of APN Activity In Vivo:** APN-ACLP (10 × 10<sup>-6</sup> M, 25 μL) was intratumorally injected in the xenograft tumor-bearing mice during anesthesia. For the inhibitor group, the xenograft tumor was directly injected with APN inhibitor BT (0.5 × 10<sup>-3</sup> M, 10 μL) at 30 min before APN-ACLP (10 × 10<sup>-6</sup> M) was intratumorally injected in the xenograft tumor-bearing mice. Then, chemiluminescence and fluorescence imaging were carried out on IVIS Spectrum imaging system (PerkinElmer, Inc.). Chemiluminescence imaging was acquired

with open filter and 40 s exposure time, and fluorescence imaging was collected with excitation at 430 nm and emission filter of 540 nm every 5 min. The SNR was calculated as  $SNR = \text{emission intensities of tumor area} / \text{background}$ , where background refers to the signal intensity of normal tissue on mice.

**Imaging and Image-Guided Resection of Tumor and Metastasis:** For imaging of tumor, after euthanasia, subcutaneous tumor and liver in the xenograft tumor-bearing mice were resected. After spraying the APN-ACL P ( $10 \times 10^{-6}$  M,  $1 \times$  PBS with 5%DMSO) onto the tissue surface, the chemiluminescence and fluorescence images were acquired using IVIS Spectrum imaging system every 10 min at 37 °C. Chemiluminescence images were captured with open filter and 20 s exposure time, and fluorescence images were captured with excitation at 430 nm and emission filter of 540 nm. For image-guided resection of orthotopic HepG2 tumor, the liver of the orthotopic HepG2 tumor-bearing mice were exposed, under anesthesia. After spraying the APN-ACL P ( $10 \times 10^{-6}$  M,  $1 \times$  PBS with 5%DMSO) for 10 min, the chemiluminescence imaging was carried out on IVIS Spectrum imaging system (PerkinElmer, Inc.), with open filter and 20 s exposure time. Then, the tumors were removed with the guidance of chemiluminescence image. For image-guided resection of hepatic and splenic metastasis, the liver and spleen with metastasis in living mice were resected. After spraying the APN-ACL P ( $10 \times 10^{-6}$  M,  $1 \times$  PBS with 5%DMSO), the chemiluminescence imaging was carried out on IVIS Spectrum imaging system (PerkinElmer, Inc.), with open filter and 20 s exposure time. Then the metastases were removed under the guidance of chemiluminescence image. For image-guided resection of peritoneal metastasis, the abdominal cavities of mice were exposed, which were sprayed by the APN-ACL P ( $10 \times 10^{-6}$  M,  $1 \times$  PBS with 5%DMSO) for 10 min and imaged by IVIS Spectrum imaging system (PerkinElmer, Inc.) with open filter and 20 s exposure time. Then the metastases were removed under the guidance of chemiluminescence imaging.

**Histology:** The organs were fixed with 4% paraformaldehyde (PFA), dehydrated in ethanol solution, and embedded in paraffin prior to 10- $\mu$ m sectioning. Histology samples were stained by hematoxylin and eosin under standard protocols. Images were acquired using a fluorescence microscope (IX73, Olympus).

**Data Analysis:** Data were expressed as the mean  $\pm$  standard deviation unless otherwise specified. The chemiluminescence and fluorescence data were quantified with ROI analysis using Living Image 4.2 Software. In vivo and in vitro chemiluminescence or fluorescence intensities were measured by ROI analysis using postprocessing vander software. Statistical comparisons between two groups were determined by t-test and more than three groups were determined by one-way ANOVA. For all tests,  $p < 0.05$  was considered statistically significant.

## Supporting Information

Supporting Information is available from the Wiley Online Library or from the author.

## Acknowledgements

Y.L. and J.Z. contributed equally to this work. The authors thank the financial support from the Natural Science Foundation of Jiangsu Province (BK20190830 and BK20190811), the National Natural Science Foundation of China (Grant No. 81901803, 81720108024, and 22106115), Jiangsu Specially Appointed Professorship, Soochow Technological Project (SYS2020082), and the Open Research Fund of State Key Laboratory of Bioelectronics, Southeast University.

## Conflict of Interest

The authors declare no conflict of interest.

## Data Availability Statement

The data that support the findings of this study are available from the corresponding author upon reasonable request.

## Keywords

activatable probes, aminopeptidase N/CD13, chemiluminescence, image-guided surgery, molecular imaging

Received: December 13, 2021

Revised: March 17, 2022

Published online:

- [1] H. H. Chu, J. H. Kim, P. N. Kim, S. Y. Kim, Y. S. Lim, S. H. Park, H. K. Ko, S. G. Lee, *Liver Int.* **2019**, *39*, 2397.
- [2] a) Y. Kawaguchi, G. Honda, I. Endo, D. Cherqui, N. Kokudo, *Liver Cancer* **2016**, *6*, 51; b) J. McMahon, C. J. O'Brien, I. Pathak, R. Hamill, E. McNeil, N. Hammersley, S. Gardiner, E. Junor, *Brit. J. Oral Maxillofac. Surg.* **2003**, *41*, 224.
- [3] Y. H. W. Derks, M. Rijpkema, H. I. V. Amadajais-Groenen, A. Kip, G. M. Franssen, J. P. M. Sedelaar, D. M. Somford, M. Simons, P. Laverman, M. Gotthardt, D. W. P. M. Löwik, S. Lütje, S. Heskamp, *Theranostics* **2021**, *11*, 1527.
- [4] a) Q. Miao, D. C. Yeo, C. Wiraja, J. Zhang, X. Ning, C. Xu, K. Pu, *Angew. Chem., Int. Ed.* **2018**, *57*, 1256; b) Q. Li, J. Zeng, Q. Miao, M. Gao, *Front. Bioeng. Biotechnol.* **2019**, *7*, 326; c) J. Huang, J. Li, Y. Lyu, Q. Miao, K. Pu, *Nat. Mater.* **2019**, *18*, 1133.
- [5] a) Y. Urano, D. Asanuma, Y. Hama, Y. Koyama, T. Barrett, M. Kamiya, T. Nagano, T. Watanabe, A. Hasegawa, P. L. Choyke, H. Kobayashi, *Nat. Med.* **2009**, *15*, 104; b) H. Kobayashi, M. Ogawa, R. Alford, P. L. Choyke, Y. Urano, *Chem. Rev.* **2010**, *110*, 2620; c) Y. Urano, M. Sakabe, N. Kosaka, M. Ogawa, M. Mitsunaga, D. Asanuma, M. Kamiya, M. R. Young, T. Nagano, P. L. Choyke, H. Kobayashi, *Sci. Transl. Med.* **2011**, *3*, 110; d) G. Hong, A. L. Antaris, H. Dai, *Nat. Biomed. Eng.* **2017**, *1*, 0010; e) K. Umezawa, M. Yoshida, M. Kamiya, T. Yamasoba, Y. Urano, *Nat. Chem.* **2017**, *9*, 279; f) H. Kubo, K. Hanaoka, Y. Kuriki, T. Komatsu, T. Ueno, R. Kojima, M. Kamiya, Y. Murayama, E. Otsuji, Y. Urano, *Sci. Rep.* **2018**, *8*, 17781; g) P. Wang, Y. Fan, L. Lu, L. Liu, L. Fan, M. Zhao, Y. Xie, C. Xu, F. Zhang, *Nat. Commun.* **2018**, *9*, 2898; h) Z. Hu, C. Fang, B. Li, Z. Zhang, C. Cao, M. Cai, S. Su, X. Sun, X. Shi, C. Li, T. Zhou, Y. Zhang, C. Chi, P. He, X. Xia, Y. Chen, S. S. Gambhir, Z. Cheng, J. Tian, *Nat. Biomed. Eng.* **2020**, *4*, 259; i) H. Li, Q. Yao, W. Sun, K. Shao, Y. Lu, J. Chung, D. Kim, J. Fan, S. Long, J. Du, Y. Li, J. Wang, J. Yoon, X. Peng, *J. Am. Chem. Soc.* **2020**, *142*, 6381; j) K. Yamamoto, S. Ohnishi, T. Mizushima, J. Kodaira, M. Ono, Y. Hatanaka, K. C. Hatanaka, Y. Kuriki, M. Kamiya, N. Ehira, K. Shinada, H. Takahashi, Y. Shimizu, Y. Urano, N. Sakamoto, *BMC Cancer* **2020**, *20*, 64; k) T. Zhao, G. Huang, Y. Li, S. Yang, S. Ramezani, Z. Lin, Y. Wang, X. Ma, Z. Zeng, M. Luo, E. de Boer, X. J. Xie, J. Thibodeaux, R. A. Brekken, X. Sun, B. D. Sumer, J. Gao, *Nat. Biomed. Eng.* **2017**, *1*, 0006; l) A. L. Vahrmeijer, M. Hutteman, J. R. van der Vorst, C. J. van de Velde, J. V. Frangioni, *Nat. Rev. Clin. Oncol.* **2013**, *10*, 507; m) M. Kamiya, Y. Urano, *Curr. Opin. Chem. Biol.* **2016**, *33*, 9.
- [6] T. Ma, Y. Hou, J. Zeng, C. Liu, P. Zhang, L. Jing, D. Shangguan, M. Gao, *J. Am. Chem. Soc.* **2018**, *140*, 211.
- [7] a) Y. Zhan, S. Ling, H. Huang, Y. Zhang, G. Chen, S. Huang, C. Li, W. Guo, Q. Wang, *Angew. Chem., Int. Ed.* **2021**, *60*, 2637; b) Q. Li, S. Li, S. He, W. Chen, P. Cheng, Y. Zhang, Q. Miao, K. Pu, *Angew. Chem., Int. Ed.* **2020**, *59*, 7018; c) D. Asanuma, M. Sakabe,

- M. Kamiya, K. Yamamoto, J. Hiratake, M. Ogawa, N. Kosaka, P. L. Choyke, T. Nagano, H. Kobayashi, Y. Urano, *Nat. Commun.* **2015**, *6*, 6463; d) J. Yoon, H. Li, D. Kim, Q. Yao, H. Ge, J. Chung, J. Fan, J. Wang, X. Peng, *Angew. Chem., Int. Ed.* **2020**, *59*, 9785; e) H. Kobayashi, P. L. Choyke, *Acc. Chem. Res.* **2011**, *44*, 83.
- [8] J. C. Widen, M. Tholen, J. J. Yim, A. Antaris, K. M. Casey, S. Rogalla, A. Klaassen, J. Sorger, M. Bogoyo, *Nat. Biomed. Eng.* **2021**, *5*, 264.
- [9] N. Hananya, D. Shabat, *Angew. Chem., Int. Ed.* **2017**, *56*, 16454.
- [10] K. Suzuki, T. Nagai, *Curr. Opin. Biotechnol.* **2017**, *48*, 135.
- [11] a) O. Green, S. Gnaim, R. Blau, A. Eldar-Boock, R. Satchi-Fainaro, D. Shabat, *J. Am. Chem. Soc.* **2017**, *139*, 13243; b) A. R. Lippert, *ACS Cent. Sci.* **2017**, *3*, 269.
- [12] X. Ni, X. Zhang, X. Duan, H. L. Zheng, X. S. Xue, D. Ding, *Nano Lett.* **2019**, *19*, 318.
- [13] a) O. Green, T. Eilon, N. Hananya, S. Gutkin, C. R. Bauer, D. Shabat, *ACS Cent. Sci.* **2017**, *3*, 349; b) J. Cao, J. Campbell, L. Liu, R. P. Mason, A. R. Lippert, *Anal. Chem.* **2016**, *88*, 4995; c) M. E. Roth-Konforti, C. R. Bauer, D. Shabat, *Angew. Chem., Int. Ed.* **2017**, *56*, 15633; d) K. J. Bruemmer, O. Green, T. A. Su, D. Shabat, C. J. Chang, *Angew. Chem., Int. Ed.* **2018**, *57*, 7508; e) J. Cao, W. An, A. G. Reeves, A. R. Lippert, *Chem. Sci.* **2018**, *9*, 2552; f) R. An, S. Wei, Z. Huang, F. Liu, D. Ye, *Anal. Chem.* **2019**, *91*, 13639; g) N. Hananya, D. Shabat, *ACS Cent. Sci.* **2019**, *5*, 949; h) S. Ye, N. Hananya, O. Green, H. Chen, A. Q. Zhao, J. Shen, D. Shabat, D. Yang, *Angew. Chem., Int. Ed.* **2020**, *59*, 14326; i) J. I. Scott, S. Gutkin, O. Green, E. J. Thompson, T. Kitamura, D. Shabat, M. Vendrell, *Angew. Chem., Int. Ed.* **2021**, *60*, 5699; j) J. Huang, Y. Jiang, J. Li, J. Huang, K. Pu, *Angew. Chem., Int. Ed.* **2021**, *60*, 3999; k) M. Ponomariov, D. Shabat, O. Green, *Bioconjugate Chem.* **2021**, *32*, 2134; l) B. Wang, Z. Chen, X. Cen, Y. Liang, L. Tan, E. Liang, L. Zheng, Y. Zheng, Z. Zhan, K. Cheng, *Chem. Sci.* **2022**, *13*, 2324.
- [14] F. M. Barnieh, P. M. Loadman, R. A. Falconer, *Biochim. Biophys. Acta, Rev. Cancer* **2021**, *1876*, 188641.
- [15] a) I. Saiki, H. Fujii, J. Yoneda, F. Abe, M. Nakajima, T. Tsuruo, I. Azuma, *Int. J. Cancer* **1993**, *54*, 137; b) H. Fujii, M. Nakajima, I. Saiki, J. Yoneda, I. Azuma, T. Tsuruo, *Clin. Exp. Metastasis* **1995**, *13*, 337; c) F. Curnis, A. Sacchi, L. Borgna, F. Magni, A. Gasparri, A. Corti, *Nat. Biotechnol.* **2000**, *18*, 1185; d) S. V. Bhagwat, N. Petrovic, Y. Okamoto, L. H. Shapiro, *Blood* **2003**, *101*, 1818; e) N. Ikeda, Y. Nakajima, T. Tokuhara, N. Hattori, M. Sho, H. Kanehiro, M. Miyake, *Clin. Cancer Res.* **2003**, *9*, 1503; f) P. Mina-Osorio, *Trends Mol. Med.* **2008**, *14*, 361; g) M. Piedfer, D. Dauzonne, R. Tang, J. N'Guyen, C. Billard, B. Bauvois, *FASEB J.* **2011**, *25*, 2831; h) X. Zhou, H. Li, C. Shi, F. Xu, Z. Zhang, Q. Yao, H. Ma, W. Sun, K. Shao, J. Du, S. Long, J. Fan, J. Wang, X. Peng, *Biomaterials* **2020**, *253*, 120089; i) J. J. Li, S. F. Chang, Liau, II, P. C. Chan, R. S. Liu, S. H. Yen, H. E. Wang, C. A. Chang, *J. Biomed. Sci.* **2016**, *23*, 15.
- [16] a) X. He, Y. Hu, W. Shi, X. Li, H. Ma, *Chem. Commun.* **2017**, *53*, 9438; b) X. He, Y. Xu, W. Shi, H. Ma, *Anal. Chem.* **2017**, *89*, 3217; c) H. Li, Y. Li, Q. Yao, J. Fan, W. Sun, S. Long, K. Shao, J. Du, J. Wang, X. Peng, *Chem. Sci.* **2019**, *10*, 1619; d) Y. Liu, C. Xu, H. W. Liu, L. Teng, S. Huan, L. Yuan, X. B. Zhang, *Anal. Chem.* **2021**, *93*, 6463; e) U. Lee, T. I. Kim, S. Jeon, Y. Luo, S. Cho, J. Bae, Y. Kim, *Chem. - Eur. J.* **2021**, *27*, 12545.
- [17] a) P. Cheng, Q. Miao, J. Huang, J. Li, K. Pu, *Anal. Chem.* **2020**, *92*, 6166; b) J. Huang, Y. Jiang, J. Li, S. He, J. Huang, K. Pu, *Angew. Chem., Int. Ed.* **2020**, *59*, 4415.
- [18] M. Yang, J. Zhang, D. Shabat, J. Fan, X. Peng, *ACS Sens.* **2020**, *5*, 3158.
- [19] L. Wu, Y. Ishigaki, Y. Hu, K. Sugimoto, W. Zeng, T. Harimoto, Y. Sun, J. He, T. Suzuki, X. Jiang, H. Y. Chen, D. Ye, *Nat. Commun.* **2020**, *11*, 446.